ACS OMEGA

Open Access

http://pubs.acs.org/journal/acsodf

Article

Efficient Photocatalytic Degradation of Congo Red Dye Using Facilely Synthesized and Characterized $MgAl_2O_4$ Nanoparticles

Eida S. Al-Farraj* and Ehab A. Abdelrahman*

Cite This: *ACS Omega* 2024, 9, 4870−4880

Read Online

ACCESS | Metrics & More | Article Recommendations

ABSTRACT: The discharge of congo red dye into water sources by factories has been associated with a range of health concerns, such as cancer, redness, skin irritation, and allergic reactions. As a result, this research focused on the cost-effective and straightforward production of $MgAl_2O_4$ nanoparticles by using the Pechini sol−gel process. Subsequently, these nanoparticles were employed for the successful photocatalytic decomposition of congo red dye. Moreover, extensive characterization of the fabricated $MgAl_2O_4$ nanoparticles was conducted through diverse methodologies, which included Fourier-transform infrared spectroscopy, ultraviolet−visible spectrophotometry, high-resolution transmission electron microscopy (HR-TEM), field-emission scanning electron microscopy (FE-SEM), and powder X-ray diffraction (XRD). Furthermore, the XRD analysis disclosed that the average crystal size of the produced $MgAl_2O_4$ nanoparticles is 10.36 nm, and their optical energy gap was determined to be 3.71 eV. The FE-SEM examination unveiled a combination of spherical and disorganized structures with a 0.14 μm average grain size. HR-TEM analysis, in turn, revealed that the fabricated $MgAl_2O_4$ nanoparticles were composed of minuscule spherical particles with an average diameter of 8.75 nm. The maximum degradation of 50 mL of congo red dye at a concentration of 25 mg/L reached 99.27% within 80 min at a pH of 3. Additionally, the findings confirmed the consistent decomposition activity toward congo red dye even after four cycles, thereby validating the effectiveness and reusability of the $MgAl_2O_4$ nanoparticles that were developed in this study.

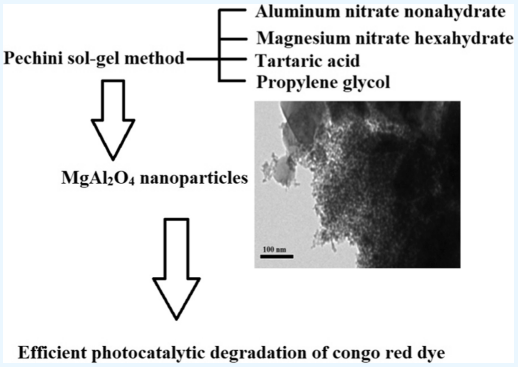

1. INTRODUCTION

Global industrialization including refineries, textiles, paper manufacturing, leather processing, plastic production, and chemicals has employed diverse organic dyes, resulting in the release of substantial amounts of harmful substances into the environment.[1−7] It is common for approximately 30−40% of these organic dyes to endure in wastewater.[8−12] Moreover, the presence of these organic dyes inhibits photosynthesis and contributes to various significant health problems for the human populace.[13−15] To tackle these issues, it is crucial to treat wastewater produced by these sectors before discharging it. Various chemical and physical methods, including coagulation, adsorption, membrane filtration, reverse osmosis, and photocatalysis, have been used to remove organic dyes from wastewater.[16−23] Among these strategies, semiconductor photocatalysis has emerged as a notably efficient method for addressing wastewater pollution. This eco-friendly, cost-effective, low-energy, and sustainable treatment approach has proven its effectiveness.[24,25] Spinel-type oxides are being recognized as promising photocatalysts with applications in the degradation of organic dyes and hydrogen production. Zinc gallate ($ZnGa_2O_4$), copper gallate ($CuGa_2O_4$), zinc ferrite ($ZnFe_2O_4$), copper aluminate ($CuAl_2O_4$), nickel ferrite ($NiFe_2O_4$), calcium bismuthate ($CaBi_2O_4$), and barium chromate ($BaCr_2O_4$) are among these oxides. They display exceptional performance in breaking down organic dyes and aiding in hydrogen generation, thanks to their distinct characteristics, such as narrow bandgaps and high catalytic efficiency.[26−32] Many techniques have been reported in the literature for producing nanosized spinel structures, which encompass Pechini sol−gel, sol−gel, microemulsion, coprecipitation, combustion, and sonochemical methods.[5,33−42] The Pechini sol−gel technique offers precise control over the composition, size, structure, and uniformity of the resulting product.[18−23] The spinel compound known as magnesium aluminate, with the chemical formula $MgAl_2O_4$, is frequently encountered. Its versatility has led to growing interest in multiple domains, including microwave dielectrics, refractory materials, humidity sensors, ceramic capacitors, structural materials for fusion reactors, and catalysis.[43] Additionally,

Received: October 26, 2023
Revised: December 28, 2023
Accepted: January 5, 2024
Published: January 19, 2024

https://doi.org/10.1021/acsomega.3c08485
ACS Omega 2024, 9, 4870−4880

Scheme 1. Procedural Steps for Producing $MgAl_2O_4$ Nanoparticles

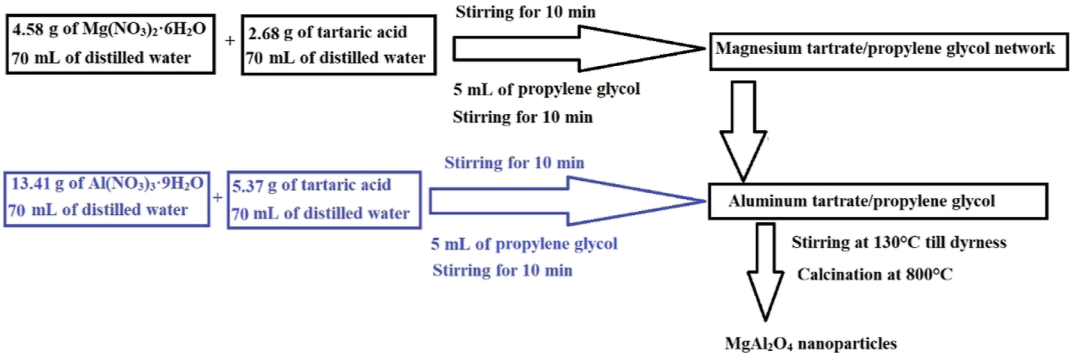

magnesium aluminate boasts advantageous properties, such as a high melting point (2135 °C), low density (3.58 g/cm^3), remarkable high-temperature strength, and outstanding resistance to chemical corrosion. Various methods have been employed for the production of magnesium aluminate, such as solid-state, spray drying, sol−gel, coprecipitation, and freeze-drying techniques.[44−48] However, most of these approaches are intricate and costly, posing challenges for large-scale production of nanosized materials when compared to Pechini sol−gel synthesis. Furthermore, these methods come with disadvantages, including the requirement of high temperatures, uneven product distribution, and limited surface area in the resulting nanosized materials. In many catalytic applications, a smaller particle size is preferred, owing to its increased surface area. Therefore, the utilization of the Pechini sol−gel technique at relatively lower temperatures offers a novel and advantageous strategy for producing nanosized magnesium aluminate particles suitable for applications in the mentioned fields, especially in the domain of photocatalysis. Congo red dye can have detrimental effects on human health, including skin irritation, redness, and potential allergic reactions. There is some research suggesting possible carcinogenic properties associated with congo red dye.[49,50] Photocatalytic decomposition of congo red dye has been studied using expensive photocatalysts such as polypyrrole/silver/graphene nanocomposite, magnetic silica-coated Ag_2WO_4/Ag_2S, chitosan/SnO_2 nanocomposite, TiO_2-doped cobalt ferrite nanoparticles, chitosan/Fe_3O_4 nanocomposite, CeO_2/CdTe nanocomposite, CeO_2/CdSe, and SnS_2/CdO nanocomposite.[51−57] In this specific study, we demonstrate the straightforward production of $MgAl_2O_4$ spinel nanoparticles through the application of the Pechini sol−gel method. The synthesized $MgAl_2O_4$ nanoparticles were characterized by using Fourier transform infrared (FT-IR), field-emission scanning electron microscopy (FE-SEM), X-ray diffraction (XRD), UV−vis, and high-resolution transmission electron microscopy (HR-TEM) analyses. Moreover, we investigated the photocatalytic decomposition of congo red dye by utilizing the prepared $MgAl_2O_4$ nanoparticles under exposure to ultraviolet radiation. Nowadays, green synthesis of nanoparticles, such as magnetite, silver, and zinc oxide, using sustainable resources is popular.[58,59] The superiority of the Pechini sol−gel method over a green synthesis approach for preparing $MgAl_2O_4$ nanoparticles might be attributed to several specific factors such as precise control, homogeneity, and scalability. The Pechini sol−gel method offers meticulous control over various parameters during the synthesis process, allowing for fine-tuning and precise manipulation of the final product. This control contributes to the uniformity, size, and structure of the $MgAl_2O_4$ nanoparticles, which can significantly affect their catalytic performance. The Pechini sol−gel method is often scalable, meaning it can be easily adapted for the production of $MgAl_2O_4$ nanoparticles on a larger scale while maintaining the desired properties. This scalability is vital for industrial applications, where large quantities of nanoparticles are required.

2. EXPERIMENTAL SECTION

2.1. Chemicals and Reagents. Propylene glycol ($C_3H_8O_2$), aluminum nitrate nonahydrate [$Al(NO_3)_3·9H_2O$], ethylenediaminetetracetic acid disodium salt dihydrate ($C_{10}H_{14}N_2Na_2O_8·2H_2O$), magnesium nitrate hexahydrate [$Mg(NO_3)_2·6H_2O$], sodium hydroxide (NaOH), tartaric acid ($C_4H_6O_6$), isopropyl alcohol (C_3H_8O), congo red dye ($C_{32}H_{22}N_6Na_2O_6S_2$), ascorbic acid ($C_6H_8O_6$), and hydrochloric acid (HCl) were purchased from the Sigma-Aldrich Company and employed in the absence of any additional refinement.

2.2. Synthesis of $MgAl_2O_4$ Nanoparticles. The synthesis of the magnesium tartrate/propylene glycol network involved the following steps: initially, 4.58 g of $Mg(NO_3)_2·6H_2O$ was dissolved in 70 mL of distilled water. Simultaneously, a tartaric acid solution was freshly prepared by dissolving 2.68 g of tartaric acid in 70 mL of distilled water. This tartaric acid solution was then added dropwise by continually stirring for a duration of 10 min. Following this, 5 mL of propylene glycol was introduced into the resultant mixture and stirred continuously for another 10 min. Similarly, the aluminum tartrate/propylene glycol network was prepared as follows: 13.41 g of $Al(NO_3)_3·9H_2O$ was dissolved in 70 mL of distilled water. A tartaric acid solution was freshly prepared by dissolving 5.37 g of tartaric acid in 70 mL of distilled water. As with the previous process, this freshly prepared tartaric acid solution was added dropwise with continuous stirring for 10 min. Subsequently, 5 mL of propylene glycol was introduced into the resultant mixture, and stirring was maintained for an additional 10 min. The next step involved combining the magnesium tartrate/propylene glycol network with an aluminum tartrate/propylene glycol network. This combination was stirred constantly at 135 °C until the mixture reached a dry state. The resulting powder was then subjected to calcination in a muffle furnace at 800 °C for a duration of 4 h, resulting in the production of $MgAl_2O_4$ nanoparticles. The key stages of fabrication of the $MgAl_2O_4$ nanoparticles are presented in Scheme 1.

2.3. Characterization. XRD analysis of the $MgAl_2O_4$ nanoparticles was performed using a D8 Advance Bruker diffractometer with an 18 kW power source and monochromated Cu K_α radiation (wavelength: 1.54 Å). The FT-IR spectrum of the $MgAl_2O_4$ nanoparticles was obtained using a

https://doi.org/10.1021/acsomega.3c08485
ACS Omega 2024, 9, 4870−4880

Scheme 2. Synthesis of $MgAl_2O_4$ Nanoparticles via the Pechini Sol−Gel Method

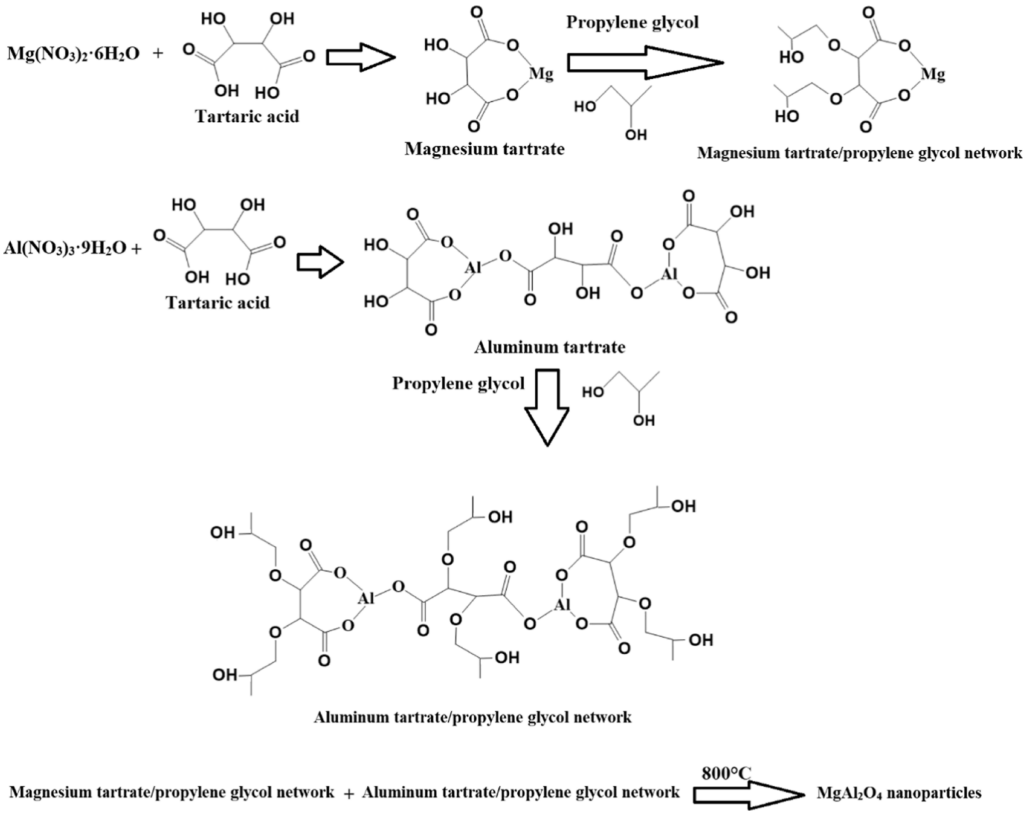

Nicolet iS50 spectrophotometer in the range of 4000−400 cm^{-1}. Besides, the surface morphology of the $MgAl_2O_4$ nanoparticles was investigated with a JSM-IT800 Schottky FE-SEM, which was equipped with an energy-dispersive X-ray (EDX) unit. A Talos F200iS HR-TEM instrument was employed to examine the morphology of the $MgAl_2O_4$ nanoparticles. Furthermore, the concentration of congo red dye was measured at 498 nm using a Shimadzu UV-1650 PC UV−vis spectrophotometer.

2.4. Photocatalytic Activity of the Synthesized $MgAl_2O_4$ Nanoparticles toward Congo Red Dye. The photocatalytic performance of $MgAl_2O_4$ nanoparticles was assessed using two identical ultraviolet lamps (wavelength = 320 nm). To begin, 50 mg of $MgAl_2O_4$ nanoparticles was introduced into 50 mL of a congo red dye solution at a concentration of 25 mg/L. This mixture was then stirred in the dark for 2 h to ensure proper dispersion of the $MgAl_2O_4$ nanoparticles and reach an adsorption/desorption equilibrium. Following this, the suspension was exposed to ultraviolet light with continuous stirring to keep the components well-mixed during irradiation. In the final step, the solution containing congo red dye was subjected to centrifugation to separate and remove the $MgAl_2O_4$ nanoparticles. Subsequently, the concentration of congo red dye in the resulting supernatant solution was determined using a UV−vis spectrophotometer at the maximum wavelength of congo red dye. Typically, the congo red dye exhibits a characteristic maximum absorption wavelength of 497 nm at a native pH 5. Besides, slight changes occur in the wavelength of the congo red dye with a change in pH, but we take this into account when calculating the concentration. Consequentially, we take the absorption value of the resulting spectrum at the maximum wavelength, even if it changes slightly, to ensure accurate results. The research investigated the effects of pH values within the range of 3−9, varying irradiation durations from 10 to 100 min, quantities of $MgAl_2O_4$ nanoparticles spanning from 0.0125 to 0.20 g, and concentrations of congo red dye ranging from 15 to 45 mg/L. Equation 1 was used to calculate the percentage of photocatalytic degradation (% P) of congo red dye achieved by the $MgAl_2O_4$ nanoparticles.

$$\% P = \frac{A_d - A_e}{A_d} \times 100 \quad (1)$$

where A_d (mg/L) indicates the determined concentration of congo red dye after the adsorption process in the dark place. A_e (mg/L) indicates the determined concentration of congo red dye after irradiation under ultraviolet conditions.

3. RESULTS AND DISCUSSION

3.1. Synthesis and Characterization of $MgAl_2O_4$ Nanoparticles. The $MgAl_2O_4$ nanoparticles were synthesized by utilizing the Pechini sol−gel technique, as illustrated in Scheme 2. First, the magnesium tartrate/propylene glycol network was created through the reaction of $Mg(NO_3)_2·6H_2O$ with tartaric acid and propylene glycol. Simultaneously, the aluminum tartrate/propylene glycol network was formed by reacting $Al(NO_3)_3·9H_2O$ with tartaric acid and propylene glycol. The next step involved combining the magnesium tartrate/propylene glycol network with the aluminum tartrate/propylene glycol network. This mixture was then heated to 130 °C until it reached a dry state. Subsequently, the resulting powder was subjected to calcination at 800 °C to yield $MgAl_2O_4$ nanoparticles. In Figure 1, the thermogravimetric analysis of the powder formed prior to calcination is depicted. The graph

https://doi.org/10.1021/acsomega.3c08485
ACS Omega 2024, 9, 4870−4880

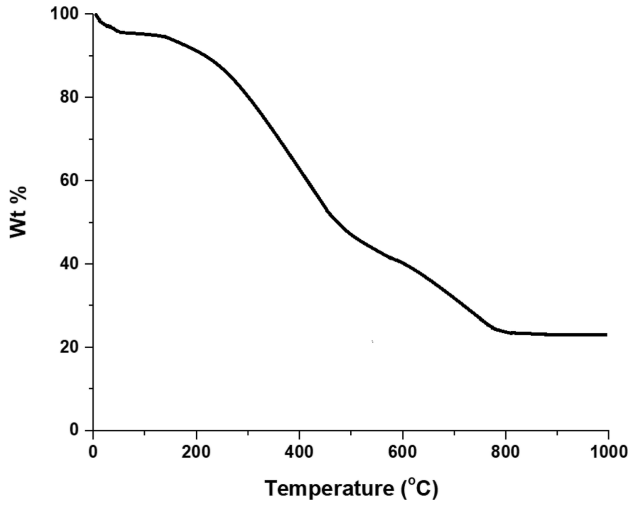

Figure 1. Thermogravimetric analysis of the precalcination powder.

clearly indicates that 800 °C is the optimal temperature for the formation of $MgAl_2O_4$ nanoparticles.

Figure 2A depicts the XRD pattern for the $MgAl_2O_4$ nanoparticles that were synthesized. It is evident from Figure 2A that each diffraction peak aligns precisely with the cubic spinel-structured $MgAl_2O_4$ with lattice parameters; a = 8.0788 Å and V_{cell} = 527.28 Å^3, as indicated by ICDD no. 021-1152.[60] Notably, no supplementary peaks corresponding to potential intermediate products such as MgO and Al_2O_3 are discernible in the pattern, affirming the pristine formation of $MgAl_2O_4$ nanoparticles. The XRD peaks observed at 2θ values of 19.08, 31.29, 36.89, 38.55, 44.89, 59.57, 65.54, and 77.75° correspond to the (111), (220), (311), (222), (400), (511), (440), and (533) diffraction planes of the $MgAl_2O_4$ nanoparticles, respectively. Furthermore, the mean crystal size of these synthesized $MgAl_2O_4$ nanoparticles is 10.36 nm. Figure 2B showcases the EDX pattern of the magnesium aluminate nanoparticles that were fabricated. The EDX analysis reveals that these magnesium aluminate nanoparticles are composed of 28.17% Al, 15.32% Mg, and 56.51% O. Notably, the absence of any other elements serves as confirmation of the high purity of the fabricated magnesium aluminate nanoparticles.

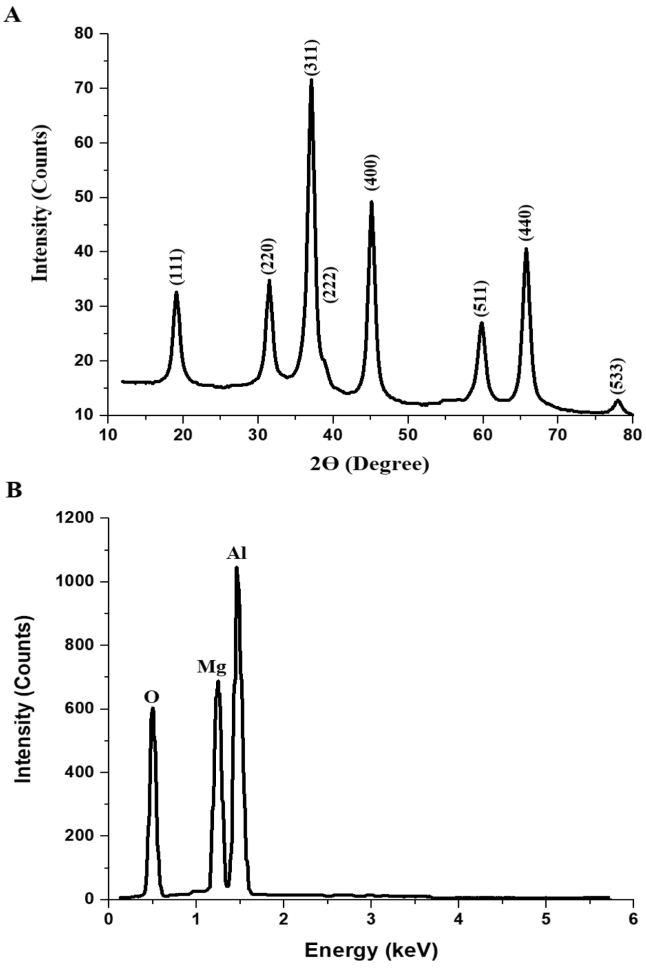

Figure 2. XRD (A) and EDX (B) analyses of the synthesized $MgAl_2O_4$ nanoparticles.

Figure 3A exhibits the FT-IR spectrum of the produced $MgAl_2O_4$ nanoparticles. The observed peaks at 527 and 696 cm^{-1} correspond to the stretching vibrations of Al−O and Mg−O bonds, respectively.[21−23,60] Additionally, the peak at 3567 cm^{-1} arises from the stretching vibrations of H−O−H, while the peak at 1628 cm^{-1} results from the bending vibrations of H−O−H.[21−23]

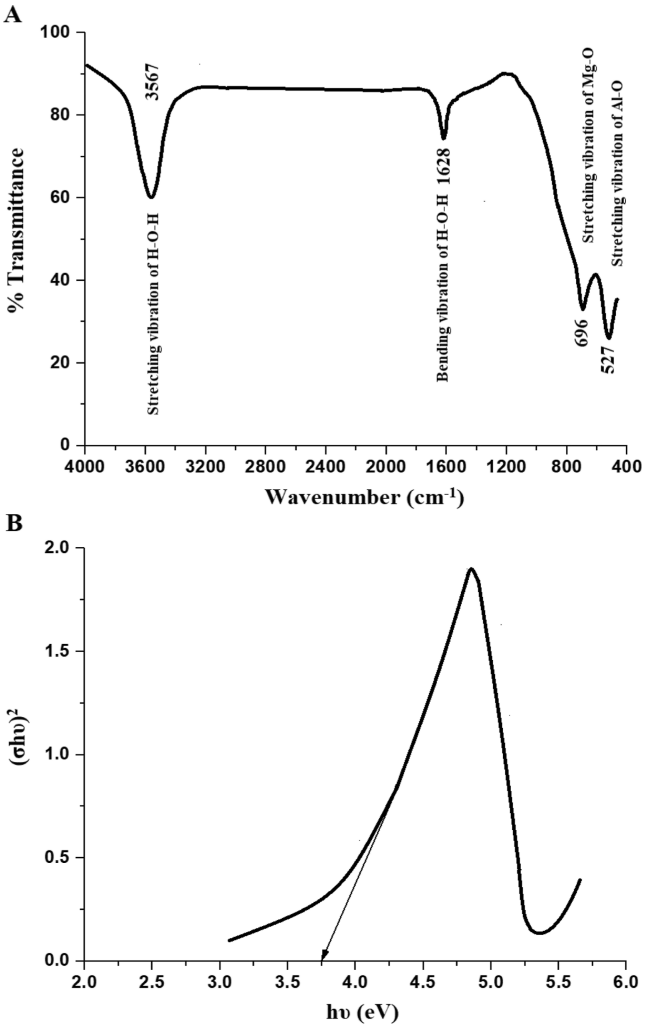

Figure 3. FT-IR analysis (A) and optical energy gap (B) of the synthesized $MgAl_2O_4$ nanoparticles.

https://doi.org/10.1021/acsomega.3c08485
ACS Omega 2024, 9, 4870−4880

To determine the optical energy gap (denoted as E_g) of the $MgAl_2O_4$ nanoparticles, eq 2 was employed. This calculation was based on their UV−vis spectra in a Nujol mull.[21−23]

$$(\sigma h\upsilon)^Y = K_E(h\upsilon - E_g) \quad (2)$$

The constant K_E represents an energy-independent factor, while σ stands for the absorption coefficient. The variable h corresponds to Planck's constant, and Y is an integer that depends on the type of electronic transition. Specifically, for direct permissible electronic transitions, Y assumes a value of 2.0, while for indirect permissible transitions, Y takes a value of 0.5. In Figure 3B, the relationship between $(\sigma h\upsilon)^2$ and $h\upsilon$ is illustrated for the synthesized $MgAl_2O_4$ nanoparticles. This graph reveals a predominance of direct permissible electronic transitions in these nanoparticles. Extrapolating the graph to the point where $(\sigma h\upsilon)^2$ reaches 0 allowed for the determination of the optical energy gap (E_g) for the $MgAl_2O_4$ nanoparticles, which was found to be 3.71 eV.

Figure 4A showcases the FE-SEM images of the produced $MgAl_2O_4$ nanoparticles. A careful examination of this image

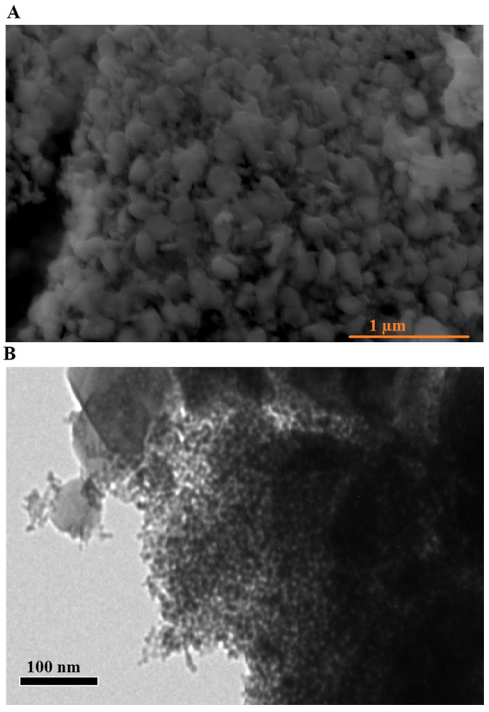

Figure 4. FE-SEM (A) and HR-TEM (B) analyses of the $MgAl_2O_4$ nanoparticles.

reveals that these nanoparticles display a mixture of spherical and disorganized shapes, with an average grain size of 0.14 μm. In Figure 4B, the image reveals that these nanoparticles are composed of small spherical particles, with an average diameter of 8.75 nm.

Figure 5 illustrates the N_2 adsorption/desorption isotherm of the $MgAl_2O_4$ nanoparticles. The results showed that the resulting curve follows the IV type, and this confirms their mesoporous nature. The surface textures, such as the Brunauer−Emmett−Teller surface area, total pore volume, and average pore size, were found to be 35.67 m^2/g, 0.1135 cc/g, and 5.65 nm, respectively.

3.2. Photocatalytic Degradation of Congo Red Dye. *3.2.1. Effect of pH.* Figure 6 illustrates the relationship between

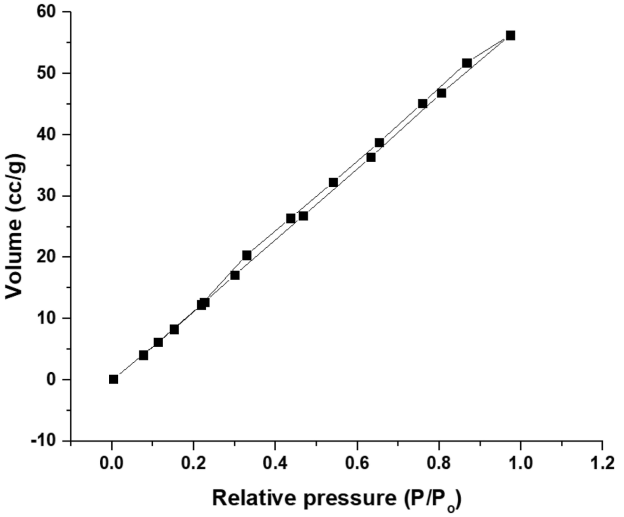

Figure 5. N_2 adsorption/desorption isotherm of the produced $MgAl_2O_4$ nanoparticles.

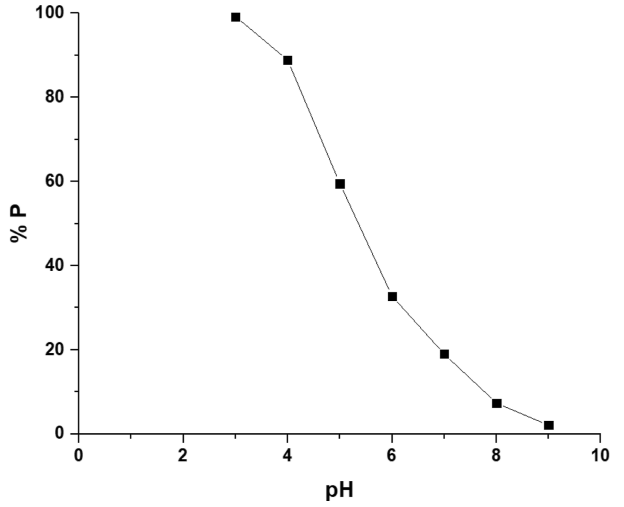

Figure 6. Effect of pH on the photocatalytic decomposition of congo red dye after exposure to ultraviolet light for 2 h.

pH and the photocatalytic degradation percentage of congo red dye when using $MgAl_2O_4$ nanoparticles under ultraviolet light conditions. It is noteworthy that when the pH of the congo red dye solution is increased from 3 to 9, there is a substantial reduction in the photocatalytic degradation percentage, decreasing from 99.22 to 2.09%. This phenomenon can be explained by the behavior of $MgAl_2O_4$ nanoparticles in different pH environments.

In an acidic medium, these nanoparticles become surrounded by positively charged hydrogen ions, which attract the anionic congo red dye, as shown in Scheme 3, resulting in an increase in the photocatalytic degradation percentage.[21−23] Conversely, in a basic medium, the presence of negatively charged hydroxide ions causes the repulsion of the anionic congo red dye, as shown in Scheme 3, leading to a decrease in the photocatalytic degradation percentage.[21−23] Therefore, a pH value of 3 is considered the optimal condition for achieving the highest photocatalytic degradation percentage of the congo red dye.

3.2.2. Effect of Exposure Time. Figure 7A illustrates the relationship that exists between the duration of ultraviolet exposure and the photocatalytic degradation percentage of

https://doi.org/10.1021/acsomega.3c08485
ACS Omega 2024, 9, 4870−4880

Scheme 3. Interactions of Congo Red Dye with $MgAl_2O_4$ Nanoparticles

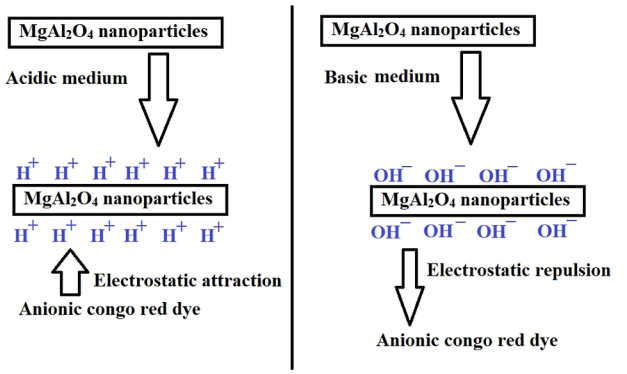

congo red dye when using $MgAl_2O_4$ nanoparticles. Extending the ultraviolet exposure time from 10 to 80 min leads to a significant increase in the photocatalytic breakdown percentage, rising from 20.06 to 99.27%. However, it was noted that further extension of the ultraviolet exposure time from 80 to 100 min had a minimal impact on the photocatalytic breakdown percentage of congo red dye, suggesting saturation of the active sites.[14−16] Consequently, 80 min is considered the optimal duration for achieving the maximum photocatalytic breakdown percentage of congo red dye. Furthermore, the photocatalytic decomposition of congo red dye follows a strong adherence to first-order kinetics, as represented by eq 3,[21−23] and this is depicted in Figure 7B.

$$\ln\frac{A_d}{A_e} = K_D t \tag{3}$$

The rate constant for first-order reactions, denoted as K_D and expressed in units of 1/min, was calculated. Upon subjecting the collected data points to linear fitting, a linear relationship with a notable correlation coefficient of 0.9867 was established, allowing for the determination of K_D, which was found to be 0.0369 1/min.

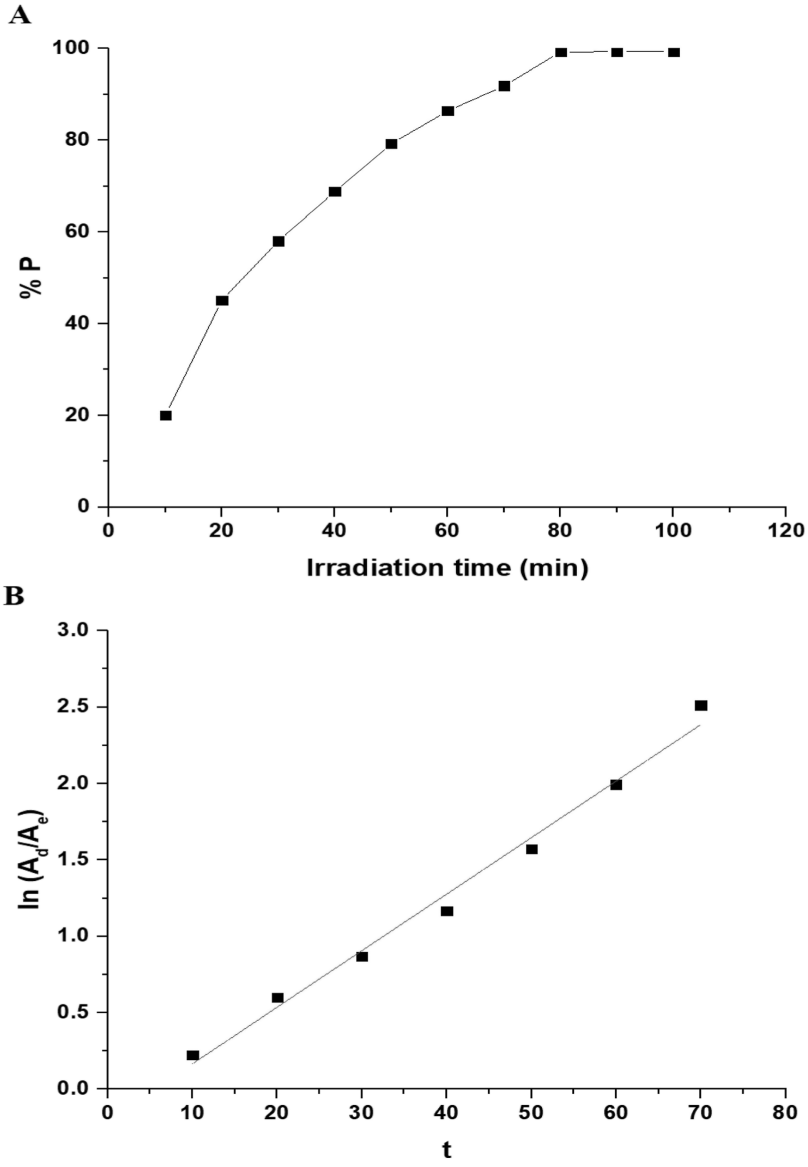

Figure 7. Effect of irradiation time on the photocatalytic decomposition of congo red dye after exposure to ultraviolet light for 2 h (A). First-order kinetic model (B).

https://doi.org/10.1021/acsomega.3c08485
ACS Omega 2024, 9, 4870−4880

The degradation rate was not dependent on the dose of the adsorbent due to the saturation of $MgAl_2O_4$. The dye that is adsorbed can saturate the available active sites on the $MgAl_2O_4$ surface. Adding more $MgAl_2O_4$ might not necessarily increase the degradation rate if the available sites are already occupied.

3.2.3. Effect of the Quantity of $MgAl_2O_4$ Nanoparticles. Figure 8 illustrates the relationship that exists between the

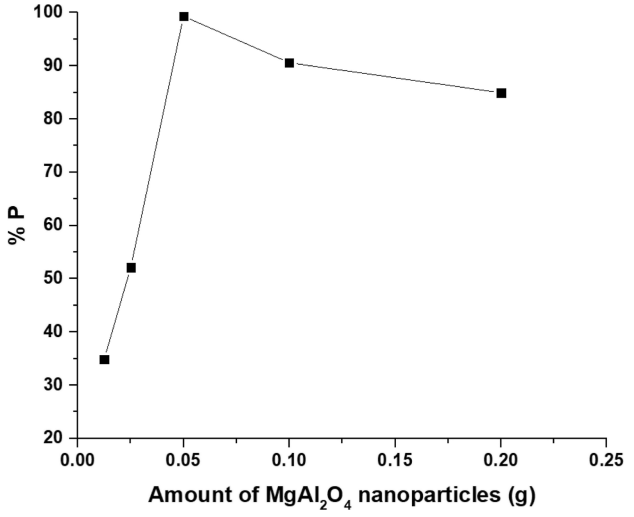

Figure 8. Effect of quantity of $MgAl_2O_4$ nanoparticles on the photocatalytic decomposition of congo red dye.

quantity of $MgAl_2O_4$ nanoparticles and the photocatalytic degradation percentage of the congo red dye. If the quantity of $MgAl_2O_4$ nanoparticles is raised from 0.0125 to 0.05 g, the photocatalytic degradation percentage of congo red dye rises from 34.86 to 99.27% due to the enhanced presence of free radicals. Conversely, if the quantity of $MgAl_2O_4$ nanoparticles is further increased from 0.05 to 0.20 g, the photocatalytic degradation percentage of congo red dye decreases from 99.27 to 84.92% because of the obstructive turbidity, which hinders the entry of ultraviolet light and reduces the population of generated free radicals.[21−23] As a result, the optimal quantity for achieving the maximum photocatalytic decomposition percentage of the congo red dye was determined to be 0.05 g.

3.2.4. Effect of Primary Congo Red Dye Concentration. Figure 9 presents the relationship that exists between the primary concentration of congo red dye and the percentage of photocatalytic degradation. If the primary concentration of congo red dye is raised from 15 to 45 mg/L, the photocatalytic degradation percentage drops from 99.55 to 60.15%. This decrease can be attributed to the reduced penetration of ultraviolet light into the $MgAl_2O_4$ nanoparticles due to the higher concentration of congo red dye.[21−23]

3.2.5. Effect of Reusability of $MgAl_2O_4$ Nanoparticles. The $MgAl_2O_4$ nanoparticles derived from the initial photocatalytic degradation experiment (first cycle) were subsequently employed in consecutive photocatalytic degradation experiments. To prepare the $MgAl_2O_4$ nanoparticles for reutilization, they underwent multiple washes with 50 mL of ethanol and 50 mL of distilled water, followed by drying at 60 °C for 1.5 h in a vacuum oven. Subsequently, the dried $MgAl_2O_4$ nanoparticles were used in a second photocatalytic degradation experiment, maintaining experimental parameters similar to those in the first cycle. Furthermore, the reusability of these $MgAl_2O_4$ nanoparticles was assessed over four repeated cycles. Figure 10

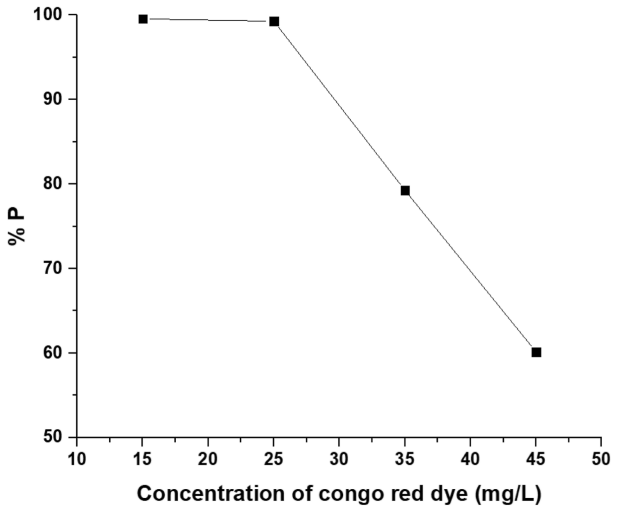

Figure 9. Effect of the primary congo red dye concentration on photocatalytic degradation.

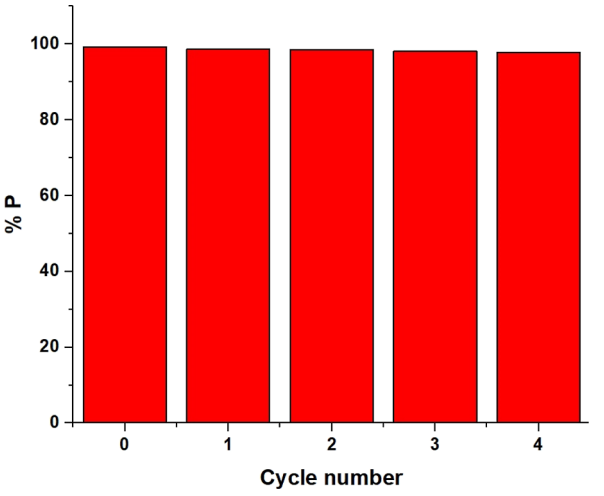

Figure 10. Effect of reusability of $MgAl_2O_4$ nanoparticles for the photocatalytic decomposition of congo red dye.

depicts the percentage of photocatalytic degradation of congo red dye plotted against the cycle number by employing the $MgAl_2O_4$ nanoparticles. Remarkably, the results revealed minimal variation in the decomposition percentage of congo red dye after four photocatalytic cycles, confirming the potency of the developed $MgAl_2O_4$ nanoparticles and their potential for repeated utilization with consistent efficiency in the degradation of congo red dye.

The claim of being able to reuse $MgAl_2O_4$ nanoparticles four times in the photodegradation process of congo red dye without a decrease in performance suggests that these nanoparticles exhibit remarkable stability and efficiency. An XRD analysis of the $MgAl_2O_4$ catalyst was performed after each use (figures omitted for brevity), and it was found that the $MgAl_2O_4$ catalyst was stable and did not change because the intensity or location of the peaks does not change. Hence, the $MgAl_2O_4$ nanoparticles possess a stable structure that endures multiple cycles of use without significant degradation or alteration in their catalytic activity.

3.2.6. Mechanism of Photocatalytic Decomposition of Congo Red Dye Utilizing $MgAl_2O_4$ Nanoparticles. The adsorption percentage of congo red dye on $MgAl_2O_4$ nano-

https://doi.org/10.1021/acsomega.3c08485
ACS Omega 2024, 9, 4870−4880

particles by electrostatic attraction at pH 3 represents a very small percentage, which is 8.28%. After that, the adsorbed congo red dye (8.28%) and the remaining congo red dye (91.72%) were photodegraded by $MgAl_2O_4$ nanoparticles, as illustrated in Scheme 4. If the $MgAl_2O_4$ nanoparticles are subjected to

Scheme 4. Mechanism of Photocatalytic Decomposition of Congo Red Dye by the $MgAl_2O_4$ Nanoparticles

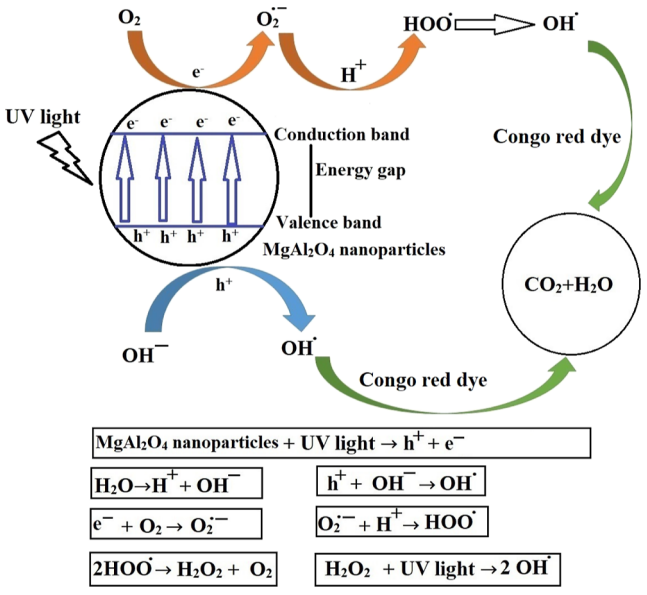

ultraviolet light, a process is initiated where electrons undergo a transition from the valence band to the conduction band. This transition leads to the generation of electrons in the conduction band and holes in the valence band. The holes created in the valence band then combine with hydroxide ions (OH^-), which is produced from the ionization of water and not from the medium, to produce hydroxyl free radicals ($OH^•$), while the electrons in the conduction band associate with oxygen (O_2) to generate oxygen anion free radicals ($O_2^{•-}$). Additionally, the oxygen anion free radicals react with hydrogen ions (H^+) to produce peroxide free radicals ($HOO^•$), which, upon exposure to ultraviolet light, transform into hydroxyl free radicals. Ultimately, these hydroxyl free radicals effectively degrade the congo red dye, converting it into harmless gases like water and carbon dioxide.[21−23] The evolution of the CO_2 gas during the degradation of congo red dye was identified using a saturated barium chloride solution, where a white barium carbonate precipitate formed.

To validate the previously proposed mechanism, a range of scavengers were introduced to assess their impact on the photocatalytic decomposition of congo red dye. Ascorbic acid was chosen as a potential scavenger for the generated electrons as well as oxygen anion free radicals, while isopropyl alcohol and ethylenediaminetetracetic acid disodium salt dihydrate were utilized as scavengers for the produced hydroxyl free radicals and holes, respectively.[21−23] The relationship between the photocatalytic degradation percentage of congo red dye and the presence of these scavengers is depicted in Figure 11A,B. The photocatalytic degradation percentage of congo red dye in the absence of any scavengers was found to be 99.27%. Conversely, when employing ascorbic acid, isopropyl alcohol, and ethylenediaminetetracetic acid disodium salt dihydrate as scavengers, the photocatalytic degradation percentages were determined to

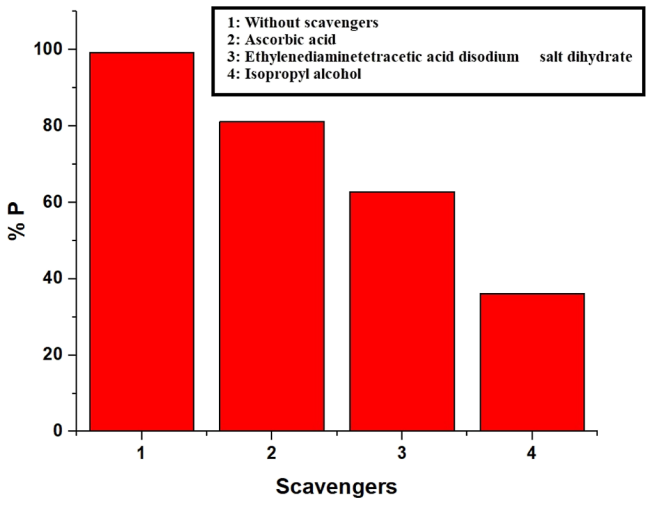

Figure 11. Effect of scavengers on the photocatalytic decomposition of congo red dye by $MgAl_2O_4$ nanoparticles.

be 81.15, 36.08, and 62.83%, respectively. These results provide clear evidence that the photocatalytic decomposition percentage of congo red dye decreases when scavengers are introduced, confirming the significance of oxygen anion free radicals, hydroxyl free radicals, holes, and electrons in the degradation process of congo red dye, as presented in Scheme 4.[21−23]

4. CONCLUSIONS

The Pechini sol−gel method, using tartaric acid as the chelating agent and propylene glycol as the cross-linker, proves to be an effective and straightforward approach for producing $MgAl_2O_4$ nanoparticles characterized by an average crystal size of 10.36 nm and an optical energy gap of 3.71 eV. The EDX analysis reveals that these magnesium aluminate nanoparticles are composed of 28.17% Al, 15.32% Mg, and 56.51% O. The observed FTIR peaks at 527 and 696 cm^{-1} correspond to the stretching vibrations of Al−O and Mg−O bonds, respectively. Additionally, the FTIR peak at 3567 cm^{-1} arises from the stretching vibrations of H−O−H, while the peak at 1628 cm^{-1} results from the bending vibrations of H−O−H. SEM analysis reveals that these nanoparticles display a mixture of spherical and disorganized shapes with an average grain size of 0.14 μm. TEM analysis revealed that these nanoparticles are composed of small spherical particles with an average diameter of 8.75 nm. If subjected to 80 min of ultraviolet irradiation, these synthesized $MgAl_2O_4$ nanoparticles demonstrated photocatalytic prowess, leading to the degradation of 99.27% of 50 mL of 25 mg/L congo red dye solution at pH 3. Notably, these $MgAl_2O_4$ nanoparticles maintained their efficiency in decomposing congo red dye even after being reused four times.

■ ASSOCIATED CONTENT

Data Availability Statement

All the data generated or analyzed during this study are incorporated in this article.

■ AUTHOR INFORMATION

Corresponding Authors

Eida S. Al-Farraj − *Department of Chemistry, College of Science, Imam Mohammad Ibn Saud Islamic University (IMSIU), Riyadh 11623, Saudi Arabia*; Email: Esalfarraj@imamu.edu.sa

https://doi.org/10.1021/acsomega.3c08485
ACS Omega 2024, 9, 4870−4880

Ehab A. Abdelrahman − *Department of Chemistry, College of Science, Imam Mohammad Ibn Saud Islamic University (IMSIU), Riyadh 11623, Saudi Arabia; Chemistry Department, Faculty of Science, Benha University, Benha 13518, Egypt;* orcid.org/0000-0003-2493-883X; Email: EAAAhmed@imamu.edu.sa

Complete contact information is available at: https://pubs.acs.org/10.1021/acsomega.3c08485

Author Contributions

Eida S. Al-Farraj—research writing and idea, Ehab A. Abdelrahman—review, idea, experimental, and research writing.

Notes

The authors declare no competing financial interest.

Ethics approval: The authors affirm that the submitted work is entirely original and has not been published elsewhere, whether in part or in its entirety, in any form, or language.

■ ACKNOWLEDGMENTS

The authors extend their appreciation to the Deputyship for Research & Innovation, Ministry of Education in Saudi Arabia for funding this research through the project number IFP-IMSIU-2023057. The authors also appreciate the Deanship of Scientific Research at Imam Mohammad Ibn Saud Islamic University (IMSIU) for supporting and supervising this project.

■ REFERENCES

(1) Gul, R.; Munir, W.; Saleh, E. A. M.; Shujah, S.; Sirajuddin, M.; Tabassum, S.; Rehman, K. u.; Khan, D.; Al-saeedi, S. I.; Abdelrahman, E. A. Ferrocene Based Schiff Bases and Their Complexes : Synthesis, Characterization and Biological Evaluation. *J. Organomet. Chem.* **2024**, *1003*, 122944.

(2) Alkhalidi, H. M.; Zaman, U.; Khan, D.; ur Rehman, K.; Omar, K. I.; Alissa, M.; Rizg, W. Y.; Bukhary, D. M.; Abdelrahman, E. A.; Refat, M. S.; Mohammed Alsuhaibani, A.; Fetooh, H. Microwave Assisted Eco-Benign Synthesis of Novel Palladium Nanoparticles (ACPs-PdNPs): A New Insight into Photocatalytic and Biomedical Applications. *J. Mol. Liq.* **2023**, *392*, 123469.

(3) Abdelrahman, E. A.; Khalil, M. M. H.; Khairy, M.; El-Reash, Y. G. A.; Gad, H. M.; Katouah, H. A.; Saad, F. A.; Rayes, S. M. E.; ur Rehman, K. Modification of Hydroxysodalite Nanoparticles by (3-Aminopropyl)Trimethoxysilane and Isatoic Anhydride as a Novel Composite for Efficient Sorption of Cu(II) Ions from Aqueous Media. *Silicon* **2023**, In press.

(4) Abdelrahman, E. A.; El-Dougdoug, W.; Kotp, Y. H. Facile Hydrothermal Synthesis of Novel Zeolite Nanostructures for the Efficient Removal of Pb(II) and Hg(II) Ions from Aqueous Media. *Silicon* **2023**, *15*, 7453−7475.

(5) Abdelrahman, E. A.; Algethami, F. K.; AlSalem, H. S.; Al-Goul, S. T.; Saad, F. A.; El-Sayyad, G. S.; Alghanmi, R. M.; Rehman, K. ur. Remarkable Removal of Pb(II) Ions from Aqueous Media Using Facilely Synthesized Sodium Manganese Silicate Hydroxide Hydrate/Manganese Silicate as a Novel Nanocomposite. *J. Inorg. Organomet. Polym. Mater.* **2023**, In press.

(6) Batool, F.; Qadir, R.; Adeeb, F.; Kanwal, S.; Abdelrahman, E. A.; Noreen, S.; Albalawi, B. F. A.; Mustaqeem, M.; Imtiaz, M.; Ditta, A.; Gondal, H. Y. Biosorption Potential of Arachis hypogaea-Derived Biochar for Cd and Ni, as Evidenced through Kinetic, Isothermal, and Thermodynamics Modeling. *ACS Omega* **2023**, *8*, 40128−40139.

(7) Kanwal, S.; Naeem, H. K.; Batool, F.; Mirza, A.; Abdelrahman, E. A.; Sharif, G.; Maqsood, F.; Mustaqeem, M.; Ditta, A. Adsorption Potential of Orange Rind−Based Nanosorbents for the Removal of Cadmium(II) and Chromium(VI) from Contaminated Water. *Environ. Sci. Pollut. Res.* **2023**, *30*, 110658−110673.

(8) Kumar, M.; Dosanjh, H. S.; Singh, H. Magnetic Zinc Ferrite−Alginic Biopolymer Composite: As an Alternative Adsorbent for the Removal of Dyes in Single and Ternary Dye System. *J. Inorg. Organomet. Polym. Mater.* **2018**, *28*, 1688−1705.

(9) Kaushal, S.; Badru, R.; Kumar, S.; Kaur, H.; Singh, P. Efficient Removal of Cationic and Anionic Dyes from Their Binary Mixtures by Organic−Inorganic Hybrid Material. *J. Inorg. Organomet. Polym. Mater.* **2018**, *28* (3), 968−977.

(10) Kumar, N.; Pandey, A.; Sharma, Y. C.; Sharma, Y. C. A Review on Sustainable Mesoporous Activated Carbon as Adsorbent for Efficient Removal of Hazardous Dyes from Industrial Wastewater. *J. Water Process Eng.* **2023**, *54*, 104054.

(11) Ahmadian, M.; Jaymand, M. Interpenetrating Polymer Network Hydrogels for Removal of Synthetic Dyes: A Comprehensive Review. *Coord. Chem. Rev.* **2023**, *486*, 215152.

(12) Kausar, A.; Zohra, S. T.; Ijaz, S.; Iqbal, M.; Iqbal, J.; Bibi, I.; Nouren, S.; El Messaoudi, N.; Nazir, A. Cellulose-Based Materials and Their Adsorptive Removal Efficiency for Dyes: A Review. *Int. J. Biol. Macromol.* **2023**, *224*, 1337−1355.

(13) Hassan, S.; Yasin, T.; Imran, Z.; Batool, S. S. Silane Based Novel Crosslinked Chitosan/Poly(Vinyl Alcohol) Membrane: Structure, Characteristic and Adsorption Behaviour. *J. Inorg. Organomet. Polym. Mater.* **2016**, *26*, 208−218.

(14) Micheletti, D. H.; da Silva Andrade, J. G.; Porto, C. E.; Alves, B. H. M.; de Carvalho, F. R.; Sakai, O. A.; Batistela, V. R. A Review of Adsorbents for Removal of Yellow Tartrazine Dye from Water and Wastewater. *Bioresour. Technol. Rep.* **2023**, *24*, 101598.

(15) Wang, S.; Ali, N. Spherical Lignin Nanostructures Synthesis, Functionalization, and Removal of Cationic Dyes. *J. Water Process Eng.* **2023**, *54*, 103924.

(16) Duan, Y.; Zhao, J.; Qiu, X.; Deng, X.; Ren, X.; Ge, W.; Yuan, H. Coagulation Performance and Floc Properties for Synchronous Removal of Reactive Dye and Polyethylene Terephthalate Microplastics. *Process Saf. Environ. Protect.* **2022**, *165*, 66−76.

(17) Ihaddaden, S.; Aberkane, D.; Boukerroui, A.; Robert, D. Removal of Methylene Blue (Basic Dye) by Coagulation-Flocculation with Biomaterials (Bentonite and Opuntia Ficus Indica). *J. Water Process Eng.* **2022**, *49*, 102952.

(18) Al-Wasidi, A. S.; Khairy, M.; Abdulkhair, B. Y.; Abdelrahman, E. A. Efficient Disposal of Basic Fuchsin Dye from Aqueous Media Using ZrO2/MgMn2O4/Mg(Mg0.333Mn1.333)O4 as a Novel and Facilely Synthesized Nanocomposite. *Inorganics* **2023**, *11*, 363.

(19) Hou, K.; Jin, K.; Fan, Z.; Du, P.; Ji, Y.; Wang, J.; Zhao, Y.; Yao, C.; Cai, Z. Facile Fabrication of Fabric-Based Membrane for Adjustable Oil-in-Water Emulsion Separation, Suspension Filtration and Dye Removal. *Sep. Purif. Technol.* **2023**, *323*, 124467.

(20) Cui, T.; Wang, X.; Chen, Y.; Chen, Y.; Fu, B.; Tu, Y. Reverse Osmosis Coupling Multi-Catalytic Ozonation (RO-MCO) in Treating Printing and Dyeing Wastewater and Membrane Concentrate: Removal Performance and Mechanism. *Water Resour. Ind.* **2023**, *30*, 100217.

(21) Abdelrahman, E. A.; Hegazey, R. M.; Ismail, S. H.; El-Feky, H. H.; Khedr, A. M.; Khairy, M.; Ammar, A. M. Facile synthesis and characterization of β-cobalt hydroxide/hydrohausmannite/ramsdellitee/spertiniite and tenorite/cobalt manganese oxide/manganese oxide as novel nanocomposites for efficient photocatalytic degradation of methylene blue dye. *Arab. J. Chem.* **2022**, *15*, 104372.

(22) Al-Kadhi, N. S.; Saad, F. A.; Shah, R. K.; El-Sayyad, G. S.; Alqahtani, Z.; Abdelrahman, E. A. Photocatalytic Decomposition of Indigo Carmine and Methylene Blue Dyes Using Facilely Synthesized Lithium Borate/Copper Oxide Nanocomposite. *J. Inorg. Organomet. Polym. Mater.* **2023**, *33*, 2765−2775.

(23) Abdelrahman, E. A.; Al-Farraj, E. S. Facile Synthesis and Characterizations of Mixed Metal Oxide Nanoparticles for the Efficient Photocatalytic Degradation of Rhodamine B and Congo Red Dyes. *Nanomaterials* **2022**, *12*, 3992.

(24) Sarkodie, B.; Amesimeku, J.; Frimpong, C.; Howard, E. K.; Feng, Q.; Xu, Z. Photocatalytic Degradation of Dyes by Novel Electrospun Nanofibers: A Review. *Chemosphere* **2023**, *313*, 137654.

(25) Ahmadi, A.; Hajilou, M.; Zavari, S.; Yaghmaei, S. A Comparative Review on Adsorption and Photocatalytic Degradation of Classified Dyes with Metal/Non-Metal-Based Modification of Graphitic Carbon Nitride Nanocomposites: Synthesis, Mechanism, and Affecting Parameters. *J. Clean. Prod.* **2023**, *382*, 134967.
(26) Boppana, V. B. R.; Doren, D. J.; Lobo, R. F. A Spinel Oxynitride with Visible-Light Photocatalytic Activity. *ChemSusChem* **2010**, *3*, 814−817.
(27) Gurunathan, K.; Baeg, J. O.; Lee, S. M.; Subramanian, E.; Moon, S. J.; Kong, K. jeong. Visible Light Active Pristine and Fe3 + Doped CuGa2 O4 Spinel Photocatalysts for Solar Hydrogen Production. *Int. J. Hydrogen Energy* **2008**, *33*, 2646−2652.
(28) Cao, S. W.; Zhu, Y. J.; Cheng, G. F.; Huang, Y. H. ZnFe2O4 Nanoparticles: Microwave-Hydrothermal Ionic Liquid Synthesis and Photocatalytic Property over Phenol. *J. Hazard. Mater.* **2009**, *171*, 431−435.
(29) Lv, W.; Liu, B.; Qiu, Q.; Wang, F.; Luo, Z.; Zhang, P.; Wei, S. Synthesis, Characterization and Photocatalytic Properties of Spinel CuAl2O4 Nanoparticles by a Sonochemical Method. *J. Alloys Compd.* **2009**, *479*, 480−483.
(30) Zhu, Z.; Li, X.; Zhao, Q.; Li, H.; Shen, Y.; Chen, G. Porous " Brick-like" NiFe2O4 Nanocrystals Loaded with Ag Species towards Effective Degradation of Toluene. *Chem. Eng. J.* **2010**, *165*, 64−70.
(31) Tang, J.; Zou, Z.; Ye, J. Efficient Photocatalytic Decomposition of Organic Contaminants over CaBi2O4 under Visible-Light Irradiation. *Angew. Chem., Int. Ed.* **2004**, *43*, 4463−4466.
(32) Wang, D.; Zou, Z.; Ye, J. A New Spinel-Type Photocatalyst BaCr2O4 for H2 Evolution under UV and Visible Light Irradiation. *Chem. Phys. Lett.* **2003**, *373*, 191−196.
(33) Al-Wasidi, A. S.; Algethami, F. K.; Saad, F. A.; Abdelrahman, E. A. Remarkable High Adsorption of Methylene Blue Dye from Aqueous Solutions Using Facilely Synthesized - MgFe2O4 Nanoparticles. *J. Inorg. Organomet. Polym. Mater.* **2023**, *33*, 2035−2045.
(34) Yanyan, J.; Jinggang, L.; Xiaotao, S.; Guiling, N.; Chengyu, W.; Xiumei, G. CuAl2O4 Powder Synthesis by Sol-Gel Method and Its Photodegradation Property under Visible Light Irradiation. *J. Sol-Gel Sci. Technol.* **2007**, *42*, 41−45.
(35) Khalifa, M. E.; Abdelrahman, E. A.; Hassanien, M. M.; Ibrahim, W. A. Application of Mesoporous Silica Nanoparticles Modified with Dibenzoylmethane as a Novel Composite for Efficient Removal of Cd(II), Hg(II), and Cu(II) Ions from Aqueous Media. *J. Inorg. Organomet. Polym. Mater.* **2020**, *30*, 2182−2196.
(36) Abdelrahman, E. A.; Khalil, M. M. H.; Algethami, F. K.; Khairy, M.; Abou El-Reash, Y. G.; Saad, F. A.; Shah, R. K.; Ammar, A. M. Facile Synthesis of MgO/CuO and MgO/Cu3MgO4 Binary Nanocomposites as Promising Adsorbents for the Disposal of Zn(II) Ions. *J. Inorg. Organomet. Polym. Mater.* **2023**, In press.
(37) Abdelrahman, E. A.; Algethami, F. K.; Alsalem, H. S.; Binkadem, M. S.; Saad, F. A.; El-Sayyad, G. S.; Raza, N.; Rehman, K. u. Facile Synthesis and Characterization of Novel Nanostructures for the Efficient Disposal of Crystal Violet Dye From Aqueous Media. *Inorganics* **2023**, *11*, 339.
(38) Abdelrahman, E. A.; Algethami, F. K.; AlSalem, H. S.; Binkadem, M. S.; Khairy, M.; Saad, F. A.; El-Sayyad, G. S.; Alqahtani, Z. Efficient Disposal of Rhodamine 6G and Acid Orange 10 Dyes from Aqueous Media Using ZrO2/CdMn2O4/CdO as Novel and Facilely Synthesized Nanocomposites. *Inorganics* **2023**, *11*, 333.
(39) Nassar, M. Y.; Ahmed, I. S.; Samir, I. A Novel Synthetic Route for Magnesium Aluminate (MgAl2O4) Nanoparticles Using Sol-Gel Auto Combustion Method and Their Photocatalytic Properties. *Spectrochim. Acta, Part A* **2014**, *131*, 329−334.
(40) Singh Yadav, R.; Kuřitka, I.; Vilcakova, J.; Jamatia, T.; Machovsky, M.; Skoda, D.; Urbánek, P.; Masař, M.; Urbánek, M.; Kalina, L.; Havlica, J. Impact of Sonochemical Synthesis Condition on the Structural and Physical Properties of MnFe2O4 Spinel Ferrite Nanoparticles. *Ultrason. Sonochem.* **2020**, *61*, 104839.
(41) Mathew, D. S.; Juang, R. S. An Overview of the Structure and Magnetism of Spinel Ferrite Nanoparticles and Their Synthesis in Microemulsions. *Chem. Eng. J.* **2007**, *129*, 51−65.
(42) Fan, Y.; Lu, X.; Ni, Y.; Zhang, H.; Zhu, M.; Li, Y.; Chen, J. Catalytic Destruction of Chlorinated Aromatic Pollutants over Mesoporous CuxMg1-XAl2O4 Spinel Oxides. *Appl. Catal., B* **2011**, *101*, 606−612.
(43) Antropova, I. G.; Budaeva, A. D.; Khomoksonova, D. P.; Batueva, S. Y.; Gulyashinov, P. A. A New Method of Obtaining Potassium Magnesium Sulfate and Magnesium Aluminate Spinel from Synnyrite, a Potassium-Rich Aluminosilicate Raw Material. *Miner. Eng.* **2022**, *187*, 107779.
(44) Basiri, A.; Nassajpour-Esfahani, A. H.; Haftbaradaran-Esfahani, M. R.; Alhaji, A.; Shafyei, A. Optimization of Spray Freeze Drying Parameters for Spark Plasma Sintering of Transparent MgAl2O4 Spinel. *Ceram. Int.* **2022**, *48*, 10751−10761.
(45) Mosayebi, Z.; Rezaei, M.; Hadian, N.; Kordshuli, F. Z.; Meshkani, F. Low Temperature Synthesis of Nanocrystalline Magnesium Aluminate with High Surface Area by Surfactant Assisted Precipitation Method: Effect of Preparation Conditions. *Mater. Res. Bull.* **2012**, *47*, 2154−2160.
(46) Gomes, S. A.; Ramaswamy, P. Plasma Sprayed Magnesium Aluminate and Alumina Composite Coatings from Waste Aluminum Dross. *Mater. Today Proc.* **2022**, *66*, 2568−2574.
(47) Habibi, N.; Wang, Y.; Arandiyan, H.; Rezaei, M. Low-Temperature Synthesis of Mesoporous Nanocrystalline Magnesium Aluminate (MgAl2O4) Spinel with High Surface Area Using a Novel Modified Sol-Gel Method. *Adv. Powder Technol.* **2017**, *28*, 1249−1257.
(48) Mukherjee, S. Development of Spinel Magnesium Aluminate by Modified Solid State Process and Its Characterization. *Mater. Today Proc.* **2022**, *67*, 314−319.
(49) Ali, I.; AL-Othman, Z. A.; Alwarthan, A. Molecular Uptake of Congo Red Dye from Water on Iron Composite Nano Particles. *J. Mol. Liq.* **2016**, *224*, 171−176.
(50) Li, Y.; Tsend, N.; Li, T. K.; Liu, H.; Yang, R.; Gai, X.; Wang, H.; Shan, S. Microwave Assisted Hydrothermal Preparation of Rice Straw Hydrochars for Adsorption of Organics and Heavy Metals. *Bioresour. Technol.* **2019**, *273*, 136−143.
(51) Punnakkal, V. S.; Anila, E. I. Polypyrrole/ Silver/Graphene Ternary Nanocomposite Synthesis and Study on Photocatalytic Property in Degrading Congo Red Dye under Visible Light. *Surface. Interfac.* **2023**, *42*, 103342.
(52) Jabbar, Z. H.; Graimed, B. H.; Issa, M. A.; Ammar, S. H.; Ebrahim, S. E.; Khadim, H. J.; Okab, A. A. Photocatalytic Degradation of Congo Red Dye Using Magnetic Silica-Coated Ag2WO4/Ag2S as Type I Heterojunction Photocatalyst: Stability and Mechanisms Studies. *Mater. Sci. Semicond. Process.* **2023**, *153*, 107151.
(53) Maruthupandy, M.; Muneeswaran, T.; Chackaravarthi, G.; Vennila, T.; Anand, M.; Cho, W. S.; Quero, F. Synthesis of Chitosan/ SnO2 Nanocomposites by Chemical Precipitation for Enhanced Visible Light Photocatalytic Degradation Efficiency of Congo Red and Rhodamine-B Dye Molecules. *J. Photochem. Photobiol., A* **2022**, *430*, 113972.
(54) Maruthupandy, M.; Muneeswaran, T.; Vennila, T.; Anand, M.; Cho, W. S.; Quero, F. Development of Chitosan Decorated Fe3O4 Nanospheres for Potential Enhancement of Photocatalytic Degradation of Congo Red Dye Molecules. *Spectrochim. Acta, Part A* **2022**, *267*, 120511.
(55) Magdalane, C. M.; Priyadharsini, G. M. A.; Kaviyarasu, K.; Jothi, A. I.; Simiyon, G. G. Synthesis and Characterization of TiO2 Doped Cobalt Ferrite Nanoparticles via Microwave Method: Investigation of Photocatalytic Performance of Congo Red Degradation Dye. *Surface. Interfac.* **2021**, *25*, 101296.
(56) Sayed, M. A.; Abo-Aly, M. M.; Abdel Aziz, A. A.; Hassan, A. A Facile Hydrothermal Synthesis of Novel CeO2/CdSe and CeO2/CdTe Nanocomposites: Spectroscopic Investigations for Economically Feasible Photocatalytic Degradation of Congo Red Dye. *Inorg. Chem. Commun.* **2021**, *130*, 108750.
(57) Srivind, J.; Nagarethinam, V. S.; Suganya, M.; Balamurugan, S.; Prabha, D.; Balu, A. R. Visible Light Irradiated Photocatalytic Performance of SnS2-CdO Nanocomposite against the Degradation

https://doi.org/10.1021/acsomega.3c08485
ACS Omega 2024, 9, 4870−4880

of Rhodamine B (Cationic) and Congo Red (Anionic) Dyes. *Mater. Sci. Eng., B* **2020**, *255*, 114530.
(58) Varadavenkatesan, T.; Pai, S.; Vinayagam, R.; Selvaraj, R. Characterization of Silver Nano-Spheres Synthesized Using the Extract of Arachis Hypogaea Nuts and Their Catalytic Potential to Degrade Dyes. *Mater. Chem. Phys.* **2021**, *272*, 125017.
(59) Vinayagam, R.; Pai, S.; Varadavenkatesan, T.; Pugazhendhi, A.; Selvaraj, R. Characterization and Photocatalytic Activity of ZnO Nanoflowers Synthesized Using Bridelia Retusa Leaf Extract. *Appl. Nanosci.* **2023**, *13*, 493−502.
(60) Sanjabi, S.; Obeydavi, A. Synthesis and Characterization of Nanocrystalline MgAl2O4 Spinel via Modified Sol-Gel Method. *J. Alloys Compd.* **2015**, *645*, 535−540.

https://doi.org/10.1021/acsomega.3c08485
ACS Omega 2024, 9, 4870−4880